



Phonon-Limited Mobility and Electron-Phonon Coupling in Lead-Free Halide Double Perovskites

Joshua Leveillee, George Volonakis, Feliciano Giustino

► To cite this version:

Joshua Leveillee, George Volonakis, Feliciano Giustino. Phonon-Limited Mobility and Electron-Phonon Coupling in Lead-Free Halide Double Perovskites. *Journal of Physical Chemistry Letters*, 2021, 12 (18), pp.4474-4482. 10.1021/acs.jpcllett.1c00841 . hal-03247358

HAL Id: hal-03247358

<https://hal.science/hal-03247358>

Submitted on 23 May 2023

HAL is a multi-disciplinary open access archive for the deposit and dissemination of scientific research documents, whether they are published or not. The documents may come from teaching and research institutions in France or abroad, or from public or private research centers.

L'archive ouverte pluridisciplinaire **HAL**, est destinée au dépôt et à la diffusion de documents scientifiques de niveau recherche, publiés ou non, émanant des établissements d'enseignement et de recherche français ou étrangers, des laboratoires publics ou privés.

Phonon-Limited Mobility and Electron-Phonon Coupling in Lead-Free Halide Double Perovskites

Joshua Leveillee,^{†,‡} George Volonakis,[¶] and Feliciano Giustino^{*,†,‡}

[†]*Oden Institute for Computational Engineering and Sciences, The University of Texas at Austin, Austin, Texas 78712, USA*

[‡]*Department of Physics, The University of Texas at Austin, Austin, Texas 78712, USA*

[¶]*Université de Rennes, ENSCR, INSA Rennes, CNRS, ISCR - UMR 6226, F-35000 Rennes, France*

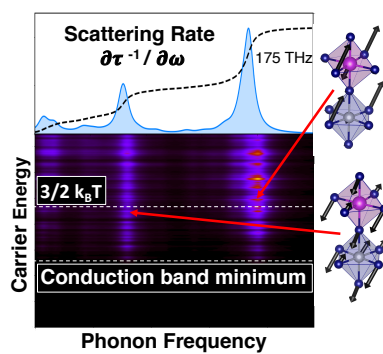
E-mail: fgiustino@oden.utexas.edu

Abstract

Lead-free halide double perovskites have attracted considerable attention as complements to lead-based halide perovskites in a range of optoelectronic applications. Experiments on $\text{Cs}_2\text{AgBiBr}_6$ indicate carrier mobilities in the range of $0.3\text{-}11\text{ cm}^2/\text{Vs}$ at room temperature, considerably lower than in lead-based perovskites. The origin of low mobilities is currently unclear, calling for an atomic-scale investigation. We report state-of-the-art *ab initio* calculations of the phonon-limited mobility of charge carriers in lead-free halide double perovskites $\text{Cs}_2\text{AgBiX}_6$ ($\text{X} = \text{Br}, \text{Cl}$). For $\text{Cs}_2\text{AgBiBr}_6$, we obtain room-temperature electron and hole mobilities of 17 and $14\text{ cm}^2/\text{Vs}$, respectively, in line with experiments. We demonstrate that the cause for the lower mobility of this compound, compared to $\text{CH}_3\text{NH}_3\text{PbI}_3$, resides in the heavier carrier effective masses. A mode-resolved analysis of scattering rates reveals the predominance of Fröhlich electron-phonon scattering, similar to lead-based perovskites. Our results

indicate that, in order to increase the mobility of lead-free perovskites, it is necessary to reduce the effective masses, for example by cation engineering.

TOC Graphic



Lead-based halide perovskites have fundamentally changed the research landscape of emerging photovoltaics over the past decade.¹⁻⁷ Devices based on the archetypal hybrid halide perovskite, $\text{CH}_3\text{NH}_3\text{PbI}_3$ (methylammonium lead tri-iodide, abbreviated as MAPI) achieved light-to-electricity power conversion efficiencies above 21%,^{8,9} related materials based on formamidinium lead-triiodide (FAPbI₃) enabled solar cells with efficiencies in excess of 25%,⁹⁻¹² and tandem perovskite-silicon solar cells reached efficiencies as high as 29%.⁹ While much progress has been made on the front of materials and device stability, in view of deploying perovskite solar cells for large-scale power generation it would be desirable to replace, or at least complement, MAPI and FAPbI₃ with more stable materials, possibly with a reduced Pb content or no Pb at all. This need has motivated the search for lead-free alternatives to MAPI and FAPbI₃ and has led to the discovery and development of lead-free halide double perovskites.¹³

Cation-ordered double-perovskite crystals, technically known as elpasolites, have been available since the early seventies,¹⁴⁻¹⁶ but their large band gaps make these compounds unsuitable as semiconductors. However, in recent years, a new family of lead-free halide double perovskites with band gaps in the visible have been designed *in silico*¹⁷⁻²⁰ and synthesized in the lab.¹⁷⁻²⁵ Among these newly synthesized compounds, $\text{Cs}_2\text{AgBiBr}_6$ has received considerable attention owing to its relatively low band gap near 2 eV. $\text{Cs}_2\text{AgBiBr}_6$ was initially reported in 2016^{17,21,22,26} as a reddish/orange crystal belonging to the $Fm\bar{3}m$ crystal space group at room temperature. Since then, $\text{Cs}_2\text{AgBiBr}_6$ has been investigated extensively as a potential new semiconductor for solar cells,²⁷⁻³³ photocatalysis,^{34,35} X-ray sensors,³⁶⁻³⁸ and photo-detectors.^{39,40} Recent work on this compound has focused on investigating cation ordering,⁴¹ the origin of its photoluminescence,⁴² and altering the A- B- or X-sites through either metal alloying,⁴³ halide mixing,⁴⁴ or by insertion of alkali metals.³⁸ The chlorine counterpart of this compound, $\text{Cs}_2\text{AgBiCl}_6$, was also discovered in 2016^{17,21,22} but has received less attention since its wider band gap makes it unsuitable for solar cell applications. Nevertheless, $\text{Cs}_2\text{AgBiCl}_6$ exhibits intriguing light emission properties,⁴⁵ and is of fundamental

interest for the understanding of tunable band gap $\text{Cs}_2\text{AgBiBr}_{6-x}\text{Cl}_x$ solid solutions.

Recent experimental work on $\text{Cs}_2\text{AgBiBr}_6$ showed that the carrier mobility of this compound is significantly lower than what is found for the prototypical lead-based perovskite MAPI. Measured values for the effective carrier mobility (averaging over electrons and holes) range between $0.3 \text{ cm}^2/\text{Vs}$ in poly-crystalline samples and $11 \text{ cm}^2/\text{Vs}$ in single crystals.^{31,46,47} These mobilities are an order of magnitude lower than in single-crystal MAPI.^{7,48-53} The origin of such a drastic reduction in mobility as compared to MAPI is an open question. Ref. 46 measured the mobility of powder samples of $\text{Cs}_2\text{AgBiBr}_6$ using time-resolved microwave conductivity, and observed that the mobility decreases with temperature as $T^{-3/2}$ between 150 K and 400 K. These data indicate that phonons play significant role in scattering carriers in this temperature range. Furthermore, measurements of temperature-dependent photoluminescence broadening showed that polar-phonon scattering is the dominant limiting factor for the lifetimes of photexcited carriers, while acoustic-phonon scattering plays a smaller role.⁵⁴ Refs. 31 and 55 performed external quantum efficiency (EQE) and time-resolved photo-luminescence (TRPL) measurements, respectively, of the carrier diffusion length in $\text{Cs}_2\text{AgBiBr}_6$, and obtained values ranging from 30 nm to 700 nm. The authors attributed this observation to defect scattering.

In order to interpret these data within a unified conceptual framework, it would be desirable to have *ab initio* parameter-free calculations of the charge transport properties of lead-free double perovskites. In particular, calculations of the phonon-limited mobility of perfect crystals will be useful to establish a theoretical upper limit for the mobility achievable in $\text{Cs}_2\text{AgBiBr}_6$ and $\text{Cs}_2\text{AgBiCl}_6$, as well as to assess the importance of individual phonons. In this work we perform predictive calculations of carrier transport in $\text{Cs}_2\text{AgBiBr}_6$ and $\text{Cs}_2\text{AgBiCl}_6$ using the state-of-the-art *ab initio* Boltzmann transport equation.⁵⁶ We find that the theoretical upper limits of the isotropic average electron and hole mobility of $\text{Cs}_2\text{AgBiBr}_6$ at room temperature are $17 \text{ cm}^2/\text{Vs}$ and $14 \text{ cm}^2/\text{Vs}$, respectively, while these limits are $7 \text{ cm}^2/\text{Vs}$ and $9 \text{ cm}^2/\text{Vs}$ for $\text{Cs}_2\text{AgBiCl}_6$, respectively. We show that the lower mobilities as

compared to MAPI stem from the heavier carrier effective masses, and that polar phonons constitute the dominant carrier scattering mechanism in these compounds.

All calculations were performed using density functional theory and density functional perturbation theory, as implemented in the Quantum ESPRESSO materials simulation suite⁵⁷ and the EPW code.⁵⁸ Technical details of the calculations are given in the Supplementary Information. The mobility tensor is determined from first principles using the linearized Boltzmann Transport Equation (BTE),⁵⁹ which describes transport at low electric fields. In this formalism, the mobility is expressed as:^{56,59,60}

$$\mu_{\alpha\beta} = \frac{1}{n\Omega} \sum_n \int \frac{d\mathbf{k}}{\Omega_{\text{BZ}}} v_{n\mathbf{k},\beta} \partial_{E_\alpha} f_{n\mathbf{k}}, \quad (1)$$

where n is the carrier density, Ω and Ω_{BZ} are the volumes of the crystal unit cell and of the Brillouin zone, respectively, $v_{n\mathbf{k},\beta}$ is the velocity of an electron with wavevector \mathbf{k} in the band n along the Cartesian direction β , and $\partial_{E_\alpha} f_{n\mathbf{k}}$ is the variation of the equilibrium carrier distribution with respect to the external electric field \mathbf{E} along the direction α . The variation $\partial_{E_\alpha} f_{n\mathbf{k}}$ is obtained as the solution of the following linear system:

$$\begin{aligned} \partial_{E_\beta} f_{n\mathbf{k}} = & e \frac{\partial f_{n\mathbf{k}}}{\epsilon_{n\mathbf{k}}} v_{n\mathbf{k},\beta} \tau_{n\mathbf{k}} + \frac{2\pi}{\hbar} \tau_{n\mathbf{k}} \sum_{m\nu} \int \frac{d\mathbf{q}}{\Omega_{\text{BZ}}} |g_{nm\nu}(\mathbf{k}, \mathbf{q})|^2 \\ & \times \left[(n_{\mathbf{q}\nu} + 1 - f_{n\mathbf{k}}^0) \delta(\epsilon_{n\mathbf{k}} - \epsilon_{m\mathbf{k}+\mathbf{q}} + \hbar\omega_{\nu\mathbf{q}}) + (n_{\mathbf{q}\nu} + f_{n\mathbf{k}}^0) \delta(\epsilon_{n\mathbf{k}} - \epsilon_{m\mathbf{k}+\mathbf{q}} - \hbar\omega_{\nu\mathbf{q}}) \right] \partial_{E_\beta} f_{m\mathbf{k}+\mathbf{q}}, \end{aligned} \quad (2)$$

where $g_{nm\nu}(\mathbf{k}, \mathbf{q})$ is the probability amplitude for the scattering between the state $n\mathbf{k}$ to the state $m\mathbf{k} + \mathbf{q}$ via a phonon of wavevector \mathbf{q} in the branch ν , and $f_{n\mathbf{k}}^0$, $n_{\mathbf{q}\nu}$ denote Fermi and Bose-Einstein occupations, respectively. The scattering rate $\tau_{n\mathbf{k}}^{-1}$ in the above expression is

calculated using the standard Fermi golden rule:

$$\begin{aligned} \tau_{n\mathbf{k}}^{-1} = & \frac{2\pi}{\hbar} \sum_{m\nu} \int \frac{d\mathbf{q}}{\Omega_{\text{BZ}}} |g_{nm\nu}(\mathbf{k}, \mathbf{q})|^2 \left[(n_{\nu\mathbf{q}} + 1 - f_{m\mathbf{k}+\mathbf{q}}^0) \delta(\epsilon_{n\mathbf{k}} - \epsilon_{m\mathbf{k}+\mathbf{q}} - \omega_{\nu\mathbf{q}}) \right. \\ & \left. + (n_{\nu\mathbf{q}} + f_{m\mathbf{k}+\mathbf{q}}^0) \delta(\epsilon_{n\mathbf{k}} - \epsilon_{m\mathbf{k}+\mathbf{q}} + \omega_{\nu\mathbf{q}}) \right], \end{aligned} \quad (3)$$

where the two terms in the square brackets represent phonon emission and absorption, respectively. In this approach, all phonons and all electron-phonon scattering processes are included on the same footing, and no *a priori* assumption is made on the relative importance of the various scattering mechanisms.⁵⁶

At room temperature, $\text{Cs}_2\text{AgBiBr}_6$ crystallizes in a cubic double perovskites structure with space group $Fm\bar{3}m$.²² Below 125 K the structure becomes tetragonal, with space group $I4/m$,⁶¹ as shown in Fig. 1(a) and (b). $\text{Cs}_2\text{AgBiCl}_6$ is also cubic at room temperature,¹⁷ but we are unaware of any attempt to study the low-temperature phases of this compound. It is reasonable to assume that a phase transition to a tetragonal structure also occurs for $\text{Cs}_2\text{AgBiCl}_6$. Indeed, our calculations of the phonon dispersion relations of $\text{Cs}_2\text{AgBiBr}_6$ and $\text{Cs}_2\text{AgBiCl}_6$ in the cubic phase show soft modes near the high-symmetry points Γ , X and W (see Supplementary Fig. S1 (a-d)). These soft modes signal structural instabilities associated with the spinning and tilting motion of the octahedra. Our calculations are consistent with a recent investigation of phonon anharmonicity in $\text{Cs}_2\text{AgBiBr}_6$.⁶² Conversely, our calculations of the phonon dispersion relations for the tetragonal phase exhibit no soft modes, as shown in Fig. 2(a) and (b), signaling that this phase is indeed the ground state structure. In order to perform mobility calculations with a well-defined phonon spectrum, we choose to work with the tetragonal phase. This choice is justified because the energy of the most important phonons is relatively unaffected by the phase transition.^{62,63}

In the tetragonal phase, $\text{Cs}_2\text{AgBiBr}_6$ and $\text{Cs}_2\text{AgBiCl}_6$ exhibit octahedral tilts designated by the $a^+a^-c^0$ Glazer notation, as seen in Fig. 1(a). The calculated lattice parameters of $\text{Cs}_2\text{AgBiBr}_6$ are $a = 8.05 \text{ \AA}$ and $c = 11.63 \text{ \AA}$, in good agreement with X-ray diffraction

measurements at 30 K⁶¹ yielding 7.89 Å and 11.34 Å, respectively. In this structure, the Bi-X-Ag bond angles in the (001) plane are 164.7° and 170.7° in Cs₂AgBiBr₆ and Cs₂AgBiCl₆, respectively. The Bi-X-Ag bonds along the *c*-axis remain at a straight angle.

Both Cs₂AgBiBr₆ and Cs₂AgBiCl₆ are indirect-gap semiconductors. Optical absorption and photoluminescence measurements indicate that the band gaps of the tetragonal and cubic phases of Cs₂AgBiBr₆ are 1.95 eV and 2.3 eV, respectively.^{22,24,31,46,61,64–66} The measured band gap of Cs₂AgBiCl₆ in the cubic phase is 2.6–2.8 eV.^{22,24,64} These data are consisted with calculations using hybrid functionals or the GW method, yielding band gaps between 1.8 eV to 2.3 eV for cubic Cs₂AgBiBr₆,^{17,67,68} and 2.7 eV for cubic Cs₂AgBiCl₆.¹⁷ In this work we describe the electronic structure at the DFT-PBE level, obtaining band gaps of 1.16 eV and 1.50 eV, respectively, in agreement with previous theoretical studies.²⁶ Figure 2(c) and (d) show that the valence band maximum and the conduction band minimum are located at the *X* and *N* points of the Brillouin zone, respectively. As in previous work, we find that the conduction band minimum is dominated by Bi-6 $p_{1/2}$ and Ag-5 s states, while the valence band maximum derives from Ag-4 $d_{3/2}$ states and Bi-6 s states. The spin-orbit interaction plays an important role in the conduction band, by splitting the lower Bi-6 $p_{1/2}$ band from the higher Bi-6 $p_{3/2}$ band by 1.6 eV.^{17,69} The projected density of states are shown in Supplementary Fig. S2(a) and (b) for completeness.

Both compounds exhibit nearly isotropic electron effective mass, and a highly anisotropic hole effective mass, as shown in Table 1. The valence band anisotropy was already noted in previous work on the cubic phases.^{17,67–70} We find that the principal axes of the effective mass tensors are aligned with the crystallographic axes of the tetragonal lattice, as expected. The effective values of the masses along these axes are $m_c^*/m_e = 0.49, 0.44$, and 0.38 for Cs₂AgBiBr₆ along the [100], [010], and [001] directions, respectively. For Cs₂AgBiCl₆ we find slightly heavier electron masses: $m_c^*/m_e = 0.66, 0.57$, and 0.50. For the hole effective masses we find $m_h^*/m_e = 1.10, 0.61$, and 0.22 for Cs₂AgBiBr₆, and $m_h^*/m_e = 0.94, 0.80$, and 0.23 for Cs₂AgBiCl₆. The lowest mass is found along the ΓX line, which corresponds to the

[100] direction. We note that, since the band extrema are found at the N and X points for the conduction bands and for the valence bands, respectively, the mass tensors have the symmetry of the small group of the wavevector at the extremum, not the symmetry of the crystal. Our calculated masses are similar to previous results for the cubic phases,^{22,70} and are a factor of 2-5 heavier than in MAPI.⁷¹

Our calculations of vibrational mode frequencies in tetragonal and cubic $\text{Cs}_2\text{AgBiBr}_6$ are in good agreement with previous non-resonant Raman scattering experiments and DFT calculations^{54,72} (see Table 2 for relevant phonon frequencies). Here, we discuss relevant phonons from high to low energy. The highest frequency mode is the IR-active asymmetric bond stretching with A_u symmetry, with an energy of 19.3 meV. Slightly lower in energy is the the highest Raman-active A_g mode, associated with metal-halogen symmetric bond stretching, with an energy of 18.7 meV. In the cubic phase, this mode blue-shifts slightly to 19.9 meV. Ref. 72 attributed exciton-phonon coupling to the interaction with this A_g mode, although here we find that the dominant coupling is to the IR-active A_u asymmetric bond stretching. At lower energy we find a Raman-active E_g symmetric stretching mode at 13.8 meV. Lower yet in energy are the Raman active octahedron tilting modes. While in the cubic phase the triple degeneracy of the tilting mode is preserved, yielding a mode with symmetry T_{2g} , this mode splits in tetragonal $\text{Cs}_2\text{AgBiBr}_6$ into a doubly-degenerate E_g mode at 7.9 meV and a non-degenerate B_g mode, at 8.3 meV. We will reference these modes as $T_{2g} \rightarrow E_g+B_g$, with the arrow indicating the symmetry-induced splitting in the tetragonal phase. Close in frequency to the $T_{2g} \rightarrow E_g+B_g$ modes is the IR-active A_u asymmetric Bi-Br-Ag bending mode at 7.8 meV. Lastly, another $T_{2g} \rightarrow E_g+B_g$ mode is present and is associated with the relative motion of the Cs cation and the halogen anions at 4.2 and 4.7 meV, respectively. Similar considerations hold for $\text{Cs}_2\text{AgBiCl}_6$, the only difference being that phonon are harder as a result of the lower mass of Cl as compared to Br, see Fig. 2(a) and (b) and Table 2, where the calculated results for the cubic phase are also presented.

Fig. 3(a) and (b) show the calculated mobility as a function of temperature for both

compounds. Our calculations indicate modest mobilities, in the range 5-19 cm²/Vs at 300 K. The electron mobility is found to be highly isotropic, while the hole mobility is strongly anisotropic, reflecting the directionality of the hole effective mass tensor. Focusing first on the isotropic average of the mobility tensor of Cs₂AgBiBr₆, we obtain a theoretical upper limit of 82±5 cm²/Vs at 100 K, decreasing to 17 cm²/Vs at 300 K. The uncertainty at low temperature indicates the estimated convergence error in the calculations (the uncertainty at room temperature is below 1 cm²/Vs).

By fitting the electron mobility of Cs₂AgBiBr₆ with a temperature power law in the range 100-400 K, we obtain $T^{-1.45}$, in good agreement with the experimental data of Ref. 46. Similar values are obtained for the hole mobility, as well as for the electron and hole mobility of Cs₂AgBiCl₆, as summarized in Table 3. A more in-depth analysis of the temperature dependence of the mobility is shown in Fig. 4(a) and (b). To eliminate the sensitivity of the temperature exponent in $\mu = aT^{-b}$ to the fitting range, we evaluate b at each temperature using $b(T) = -d \log \mu / d \log T$. From Fig. 4 we see that the exponent exhibits a significant variation with temperature (between 1.1 and 1.9), indicating that more than one group of phonons contributes significantly to carrier scattering. The temperature exponent in Fig. 4 is relatively close to $b = 3/2$, which usually is indicative of deformation potential scattering by acoustic or optical phonons. However, in the case of MAPI, where the temperature exponent is also close to $b = 3/2$,^{7,53} the dominant scattering mechanism was established to be polar phonon scattering.

In order to quantify the relative importance of various groups of phonons in the mobility of Cs₂AgBiBr₆ and Cs₂AgBiCl₆, we show in Fig. 5(a) and (b) a spectral decomposition of the electron scattering rate as a function of phonon energy. The electron scattering rates are evaluated for the characteristic carrier energy of $3k_B T/2$.⁵³ The corresponding data for the hole mobility are shown in Supplementary Fig. S3a and S3b. For both compounds we recognize two prominent broad peaks [labeled (a1), (a2) for Cs₂AgBiBr₆ and (b1), (b2) for Cs₂AgBiCl₆]. In order to assign these peaks, we perform a decomposition in terms of the

normal modes of a regular octahedron,⁷³ as described in the Supplementary Information. Group (a1) of $\text{Cs}_2\text{AgBiBr}_6$ consists of the A_u asymmetric Bi-Br stretching mode at 19.3 meV, as shown in Fig. 5(d), and the A_g symmetric Bi-Br stretching mode at 18.7 meV. While the broad peaks contain contributions from both symmetric and asymmetric bond stretching, the peaks is centered predominantly on the A_u asymmetric stretching mode with only a minor contribution from the A_g symmetric stretching mode. Group (a2) consists of the A_u asymmetric Ag-Br bending mode at 7.8 meV, as shown in Fig. 5(c), and the $T_{2g} \rightarrow B_g + E_g$ Raman modes, where the arrow indicates the splitting of the T_{2g} mode under the cubic to tetragonal phase transition. The contribution to the total scattering rate from these modes amounts to $\sim 70\%$ of the total, while acoustic phonons account for $\sim 10\%$ of the total rate. Similar considerations hold for $\text{Cs}_2\text{AgBiCl}_6$. A breakdown of mode contribution to the electron scattering rates is given in Table 4.

In Fig. 5 we also show as dot-dashed lines the scattering rate calculated after eliminating the long-range Fröhlich electron-phonon interaction,⁷⁴ while retaining the scattering by transverse-optical phonons and acoustic phonons. From this comparison it is clear that long-range Fröhlich coupling completely dominates the scattering rate, accounting for more than 80% of the total rate in both compounds. This finding firmly establishes polar optical phonon scattering as the main source of carrier relaxation in lead-free halide double perovskites.

For comparison, our calculated scattering rates of 175 THz for $\text{Cs}_2\text{AgBiBr}_6$ and 146 THz for $\text{Cs}_2\text{AgBiCl}_6$ are slightly lower than in MAPI, 180 THz.⁵³ These rates closely reflects the thermal populations of the LO phonons in these compounds, with MAPI having the largest Bose-Einstein factor as a result of its lowest LO phonon energy (12 meV). For completeness we report in Table 5 the calculates scattering rates for electrons and holes in both compounds as well as previously reported data for MAPI.

It is instructive to compare the mobility of $\text{Cs}_2\text{AgBiBr}_6$, $\text{Cs}_2\text{AgBiCl}_6$, and MAPI using a simple Drude model. In this model the mobility is given by $\mu^D = e\tau/m^*$, where τ is

an effective scattering rate and m^* an isotropic carrier effective mass (see Supplementary Information for the definition of average mass). Using our *ab initio* calculations of the effective masses and scattering rates, we obtain $\mu^D = 23, 21$, and $47 \text{ cm}^2/\text{Vs}$ for electrons in $\text{Cs}_2\text{AgBiBr}_6$, $\text{Cs}_2\text{AgBiCl}_6$, and MAPI, respectively (data for MAPI are from Ref. 53). These values are in qualitative agreement with the mobilities calculated using the *ab initio* BTE, $\mu^{\text{BTE}} = 16.7, 7.1$ and $76 \text{ cm}^2/\text{Vs}$, respectively (the MAPI result is based on the SERTA approximation, Ref. 53). Similar observations hold for holes, as shown in Table 5. Overall, this comparison shows that, albeit not predictive, the Drude model is appropriate for interpreting order-of-magnitude trends in the transport properties of these perovskites.

Our present analysis establishes that the lower mobility of lead-free halide double perovskites, as compared to MAPI, originates from the heavier carrier effective masses. The harder phonons of $\text{Cs}_2\text{AgBiBr}_6$ and $\text{Cs}_2\text{AgBiCl}_6$ as compared to MAPI contribute to slightly lowering the carrier scattering rates, but this effect only partially compensates for the heavier masses. These considerations also allow us to estimate how the tetragonal-to-cubic phase transition would affect the mobility of $\text{Cs}_2\text{AgBiBr}_6$ and $\text{Cs}_2\text{AgBiCl}_6$. Considering the effective masses along the $[100]$ direction, the electron and hole effective masses of $\text{Cs}_2\text{AgBiBr}_6$ and $\text{Cs}_2\text{AgBiCl}_6$ are approximately 30% lighter in the cubic phase as compared to the tetragonal phase.^{17,22,70} Similarly, the highest LO phonons are $\sim 5\%$ harder in the cubic phase. Using these values in the simplified Drude model, and assuming that the scattering rate is proportional to $2n + 1$, with n being the Bose-Einstein occupation of the highest-energy LO modes, we find that the room-temperature mobility could increase by 50% from the tetragonal to the cubic phase in both $\text{Cs}_2\text{AgBiBr}_6$ and $\text{Cs}_2\text{AgBiCl}_6$.

In conclusion, we investigated the carrier mobility of the lead-free halide double perovskites $\text{Cs}_2\text{AgBiBr}_6$ and $\text{Cs}_2\text{AgBiCl}_6$ using the *ab initio* Boltzmann transport equation. Our calculations using the low-temperature tetragonal phase indicate that the theoretical upper limit of the intrinsic mobility of $\text{Cs}_2\text{AgBiBr}_6$ is $17 \text{ cm}^2/\text{Vs}$ at room temperature, and a simple estimate indicates that this value could increase to $25 \text{ cm}^2/\text{Vs}$ in the cubic phase.

We attribute the origin of the lower mobility as compared to lead-based perovskites such as MAPbI₃ to the heavier carrier effective masses, and we show that the predominant scattering mechanism is the Fröhlich interaction. Based on our results, the most direct route to improving the mobility of Cs₂AgBiBr₆ would be to reduce the carrier effective masses. Metallic cation and halogen anion substitution and alloy engineering are promising routes to tune the electronic band dispersions. It has been demonstrated in theoretical investigations that the choice of halogen anion and metallic cations strongly changes the effective masses of double-perovskite crystals, with iodine-based compounds exhibiting the lightest effective masses.¹⁷ Band structure engineering by halogen substitution has already been realized in Cs₂AgBiBr₆ by alloying to Cs₂AgBiBr_{6-x}Cl_x.⁶⁴ Future efforts to partially substitute Br with I could reduce the hole effective masses and increase hole mobility. Additionally, cation engineering by alloying with In substituting for Bi in Cs₂AgBi_{1-x}In_xBr₆ has been recently demonstrated.⁷⁵ Combinations of these efforts could realize a path towards higher mobility lead-free double perovskite solar cells.

Acknowledgement

This work is primarily supported by the Computational Materials Sciences Program funded by the U.S. Department of Energy, Office of Science, Basic Energy Sciences, under Award No. DE-SC0020129. Support by the Robert A. Welch Foundation under award number F-1990-20190330 is also acknowledged. The authors acknowledge the Texas Advanced Computing Center (TACC) at The University of Texas at Austin for providing HPC resources, including the Frontera and Lonestar5 systems, that have contributed to the research results reported within this paper. URL: <http://www.tacc.utexas.edu>. This research used resources of the National Energy Research Scientific Computing Center, a DOE Office of Science User Facility supported by the Office of Science of the U.S. Department of Energy under Contract No. DE-AC02-05CH11231.

Table 1: Calculated eigenvalues of the effective mass tensors, ellipsoidal effective mass averages, and anisotropy ratios (see Supplemental Information) in tetragonal $\text{Cs}_2\text{BiAgX}_6$, $\text{X} = \text{Br}, \text{Cl}$. Literature values are calculated on the $Fm\bar{3}m$ cubic cell with the LDA exchange-correlation functional.^{17,70}

	<u>Holes</u>			Average	Anisotropy
	$m_{h,1}$	$m_{h,2}$	$m_{h,3}$		
$\text{Cs}_2\text{AgBiBr}_6$	0.22	0.61	1.10	0.42	49%
Literature	0.14, ⁷⁰ 0.15 ¹⁷	0.57 ¹⁷	-	-	50% ¹⁷
$\text{Cs}_2\text{AgBiCl}_6$	0.23	0.80	0.90	0.45	45%
Literature	0.15, ⁷⁰ 0.16 ¹⁷	0.63 ¹⁷	-	-	49% ¹⁷
	<u>Electrons</u>			Average	Anisotropy
	$m_{e,1}$	$m_{e,2}$	$m_{e,2}$		
$\text{Cs}_2\text{AgBiBr}_6$	0.38	0.44	0.49	0.43	10%
Literature	0.28, ¹⁷ 0.38 ⁷⁰	0.48 ¹⁷	-	-	27% ¹⁷
$\text{Cs}_2\text{AgBiCl}_6$	0.50	0.57	0.66	0.57	11%
Literature	0.34, ¹⁷ 0.43 ⁷⁰	-	-	-	0% ¹⁷

Table 2: Comparison between the calculated energies of Raman-active A_g , E_g , $T_{2g} \rightarrow B_g + E_g$ modes and experiments, and calculated IR-active stretching and bending A_u modes (in meV) in $\text{Cs}_2\text{AgBiX}_6$ with $X=\text{Br,Cl}$. The arrow indicates the splitting of the triply degenerate T_{2g} modes of the cubic phase into a doubly degenerate E_{2g} modes and a B_g mode in the tetragonal phase. Previous calculations were performed in the cubic $Fm\bar{3}m$ unit cell with the LDA exchange-correlation functional.⁷²

Raman-Active	A_g	E_g	$T_{2g} \rightarrow B_g + E_g$	$T_{2g} \rightarrow B_g + E_g$
Tetragonal				
$\text{Cs}_2\text{AgBiBr}_6$	18.6	13.8	7.9, 8.3	4.2, 4.7
$\text{Cs}_2\text{AgBiCl}_6$	30.1	21.7	12.8, 12.9	4.5, 4.7
Cubic				
$\text{Cs}_2\text{AgBiBr}_6$	19.9	14.6	7.7	4.6
$\text{Cs}_2\text{AgBiBr}_6$ (exp.)	22.0, ⁷⁶ 21.9, ⁷² 21.7 ⁵⁴	16.7 ⁵⁴	9.3 ⁵⁴	5.0 ⁵⁴
$\text{Cs}_2\text{AgBiBr}_6$ (theory) ⁷²	20.9	16.0	7.4	2.7
$\text{Cs}_2\text{AgBiCl}_6$	31.6	22.3	12.5	4.6
IR-Active	A_u stretch	A_u bend		
Tetragonal				
$\text{Cs}_2\text{AgBiBr}_6$	19.3	7.8		
$\text{Cs}_2\text{AgBiCl}_6$	28.1	10.5		
Cubic				
$\text{Cs}_2\text{AgBiBr}_6$	20.1	7.5		
$\text{Cs}_2\text{AgBiCl}_6$	30.0	10.5		

Table 3: Calculated carrier mobilities and temperature exponent b in $\mu = aT^{-b}$ for tetragonal $\text{Cs}_2\text{AgBiBr}_6$ and $\text{Cs}_2\text{AgBiCl}_6$ at $T = 300$ K. Cartesian directions x , y , and z align with crystalline directions $[100]$, $[010]$, and $[001]$ as shown in Fig. 1(a). The subscript “iso” indicates the isotropic average.

	$\text{Cs}_2\text{AgBiBr}_6$		$\text{Cs}_2\text{AgBiCl}_6$	
	Electrons	Holes	Electrons	Holes
$\mu_{x,y}$	16.2	18.7	7.1	10.9
μ_z	17.3	5.2	7.1	6.4
μ_{iso}	16.7	14.2	7.1	9.4
$b_{x,y}$	1.41	1.38	1.81	1.64
b_z	1.42	1.53	1.81	1.38
b_{iso}	1.41	1.43	1.81	1.55

Table 4: Relative contribution to the electron scattering rates from the various phonon modes in tetragonal $\text{Cs}_2\text{AgBiBr}_6$ and $\text{Cs}_2\text{AgBiCl}_6$. Values are determined as integrals over the intervals of the frequency axis partitioned into regions containing the various contributions (shown under % contributions, in meV). The % contribution from polar modes are determined by integrating over the the scattering rate calculated from the long-range Fröhlich electron-phonon matrix element over the entire frequency range. The difference between the full scattering rate and the polar scattering rate determines the non-polar contribution. The arrow indicates the splitting of the cubic triply degenerate T_{2g} modes into a doubly degenerate E_{2g} modes and a B_g mode in the tetragonal system.

Phonon group	$\text{Cs}_2\text{AgBiBr}_6$	$\text{Cs}_2\text{AgBiCl}_6$
A_u polar and A_g non-polar stretching	49%	44%
Integration range (meV)	17.5 - 25.0	25.0 - 33.0
A_u polar and $T_{2g} \rightarrow B_g + E_g$ non-polar bending	21%	28%
Integration range (meV)	6.0 - 9.1	7.5 - 15.1
Acoustic	11%	9%
Integration range (meV)	0.0 - 2.5	0.0 - 2.5
Remainder	19%	19%
Total polar	83%	85%
Total non-polar	17%	15%

Table 5: Comparison between theoretical Drude Model and BTE relaxation times, ellipsoidal-averaged effective masses, and mobilities in Bi-metal halide double perovskites, hybrid metal halide perovskite MAPbI₃,⁵³ and GaN.⁷⁷ The average τ^{-1} , in THz, are calculated by integrating $\partial\tau^{-1}/\partial\omega$ at an energy of $3/2k_B T$ away from the band edge. Direction-averaged effective masses m^* are in units of the electron rest mass, and mobilities μ are in units of cm²/Vs.

	Electrons				Holes			
	τ_e^{-1}	$m_{\text{ave},e}^*$	$\mu_{\text{Drude},e}$	$\mu_{\text{IBTE},e}$	τ_h^{-1}	$m_{\text{ave},h}^*$	$\mu_{\text{Drude},h}$	$\mu_{\text{IBTE},h}$
Cs ₂ AgBiBr ₆	175.4	0.43	23.3	16.7	275.9	0.42	15.2	14.2
Cs ₂ AgBrCl ₆	146.2	0.57	21.1	7.1	195.8	0.45	19.9	9.4
MAPbI ₃ ⁵³	180	0.21	46.5	76	-	-	-	-
GaN ⁷⁷	16	0.20	550	905	-	-	-	-

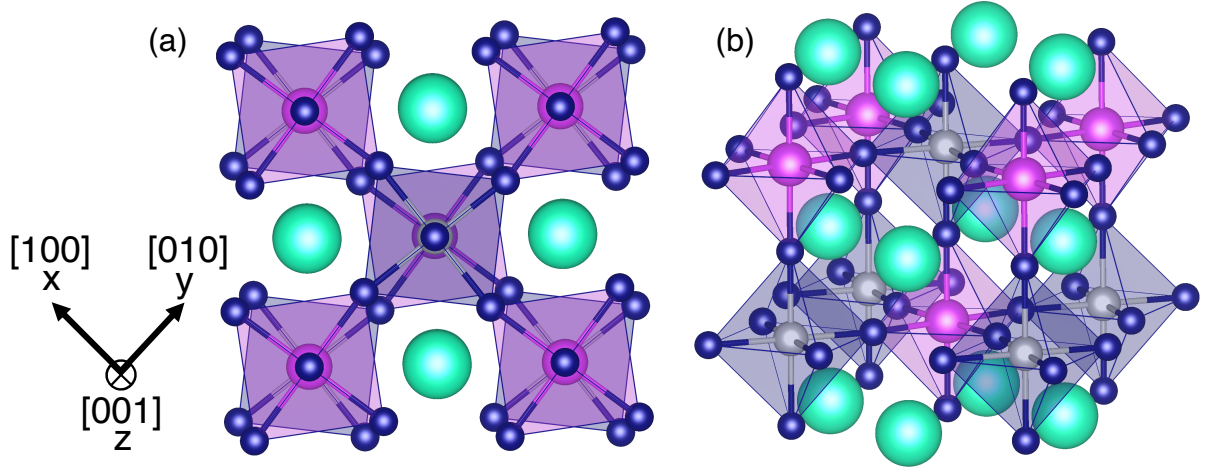


Figure 1: Atomic structure of tetragonal lead-free halide double perovskite $\text{Cs}_2\text{AgBiX}_6$, with $\text{X}=\text{Br}$ or Cl . The metal cations Ag (silver) and Bi (purple) are positioned at the centers of the octahedra. The vertices of the octahedra are the location of the halogen anions (navy blue). The A-site cations Cs (in light green) are positioned in the inter-octahedron vacancies. Sub-figure (a) shows the projection along the $[001]$ (z) direction (out-of-page) with the tetragonal crystalline axes $[100]$ (x) and $[010]$ (y) indicated by the inset arrows while (b) shows a general 3D view of the same crystal structure.

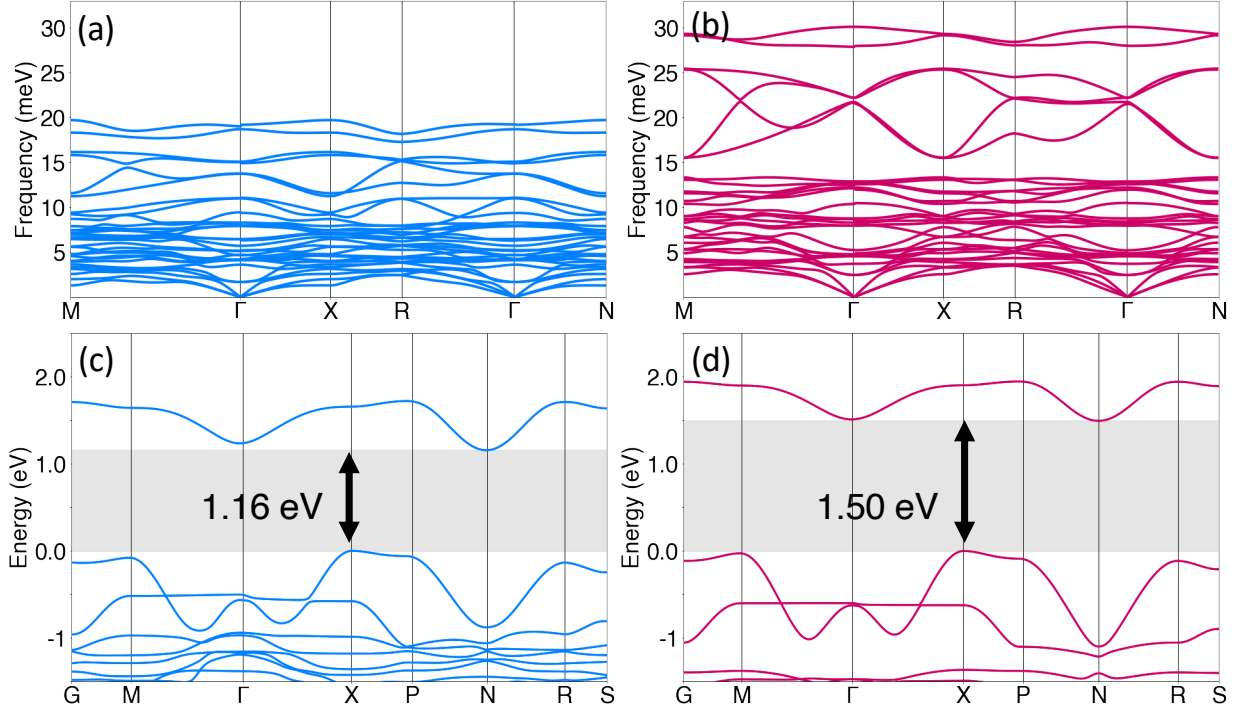


Figure 2: The phonon and electronic band structures of (a,c) tetragonal $\text{Cs}_2\text{AgBiBr}_6$ and (b,d) tetragonal $\text{Cs}_2\text{AgBiCl}_6$.

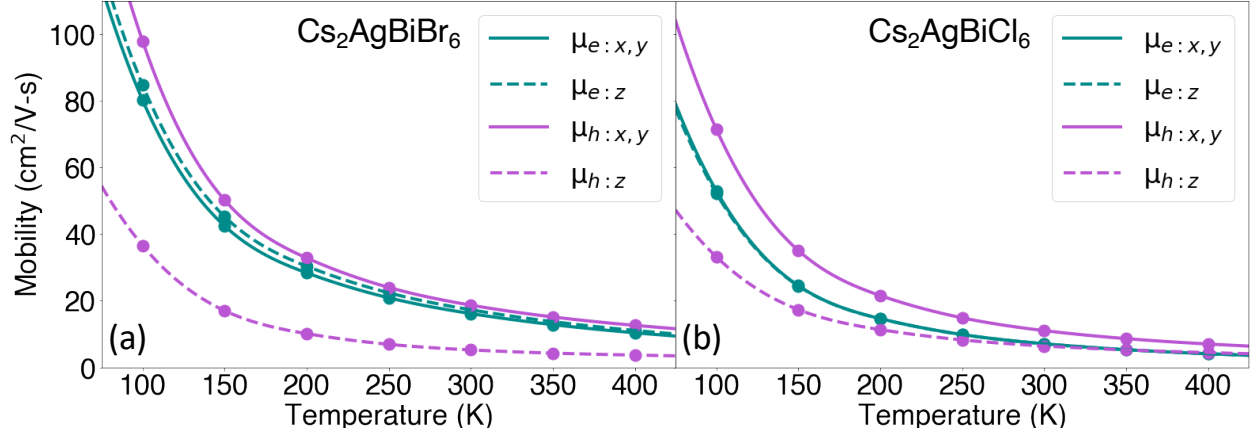


Figure 3: Calculated temperature-dependent phonon-limited mobilities in tetragonal $\text{Cs}_2\text{AgBiBr}_6$ (a) and tetragonal $\text{Cs}_2\text{AgBiCl}_6$ (b), along the three Cartesian directions shown in Fig. 1. Green dots indicate electron mobilities calculated in the x,y (solid) and z (dashed) directions, and violet dots indicate hole mobilities calculated in the x,y (solid) and z (dashed) directions. The lines are guides to the eye.

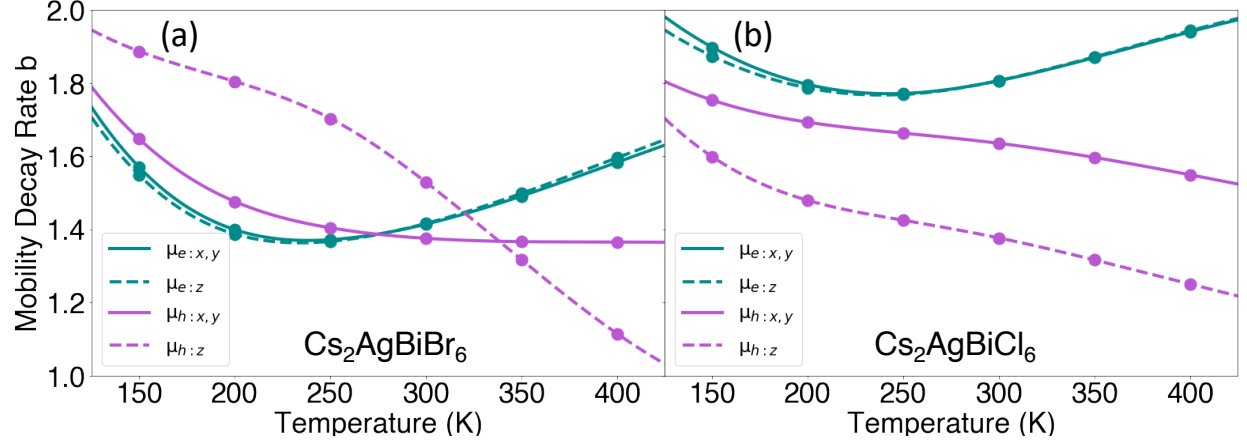


Figure 4: Temperature exponent of the mobility, $b = \Delta \ln \mu / \Delta \ln T$, for electrons (blue) and holes (red) in the x , y (solid) and z (dashed) directions of tetragonal $\text{Cs}_2\text{AgBiBr}_6$ (a) and tetragonal $\text{Cs}_2\text{AgBiCl}_6$ (b). The lines are guides to the eye. The variations are taken with respect to the values at 100 K, using increments of 50 K.

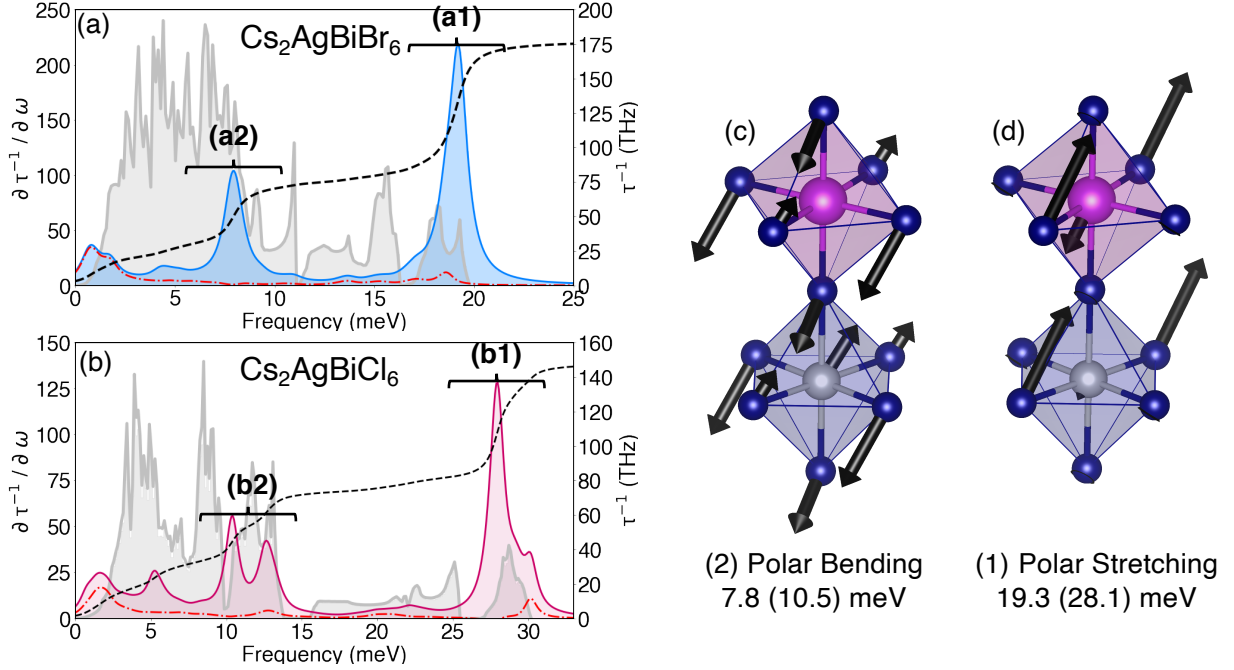


Figure 5: (a and b) (solid line, shaded) Energy-resolved electron-phonon scattering rate $\partial\tau^{-1}/\partial\omega$ at a carrier energy of $3/2k_B T$ above the conduction band minimum in (a, blue) $\text{Cs}_2\text{AgBiBr}_6$ and (b, pink) $\text{Cs}_2\text{AgBiCl}_6$. The phonon density of states is shown in grey in the background for both materials. The black dashed line shows the integrated electron scattering rate τ^{-1} , which equates to a total 175.4 THz in $\text{Cs}_2\text{AgBiBr}_6$ and 146.2 THz in $\text{Cs}_2\text{AgBiCl}_6$. The dot-dashed red line indicates the short-range non-polar contributions to the frequency resolved scattering rate. The bracketed regions (a1) and (b1) indicate the energy ranges dominated by scattering from the IR-active A_u Bi-X stretching mode and the Raman-active A_g non-polar Bi-X-Ag stretching mode. The bracketed regions (a2) and (b2) indicate the energy ranges dominated by the IR-active A_u Bi-X-Ag bond bending modes and the Raman-active T_{2g} (split into E_g and A_g in the tetragonal system) non-polar Bi-X-Ag bond bending modes. (c) and (d) show schematics of the IR-active A_u Bi-X-Ag bending mode and IR-active A_u polar Bi-X-Ag stretching mode, respectively. The halogen atoms are shown in dark blue, Bi in pink, and Ag in gray. The phonon energies of these modes are displayed for $\text{Cs}_2\text{AgBiBr}_6$ ($\text{Cs}_2\text{AgBiCl}_6$). These two groups of modes are the dominant contributors to the carrier scattering rate.

Supporting Information Available

Supporting information detailing computational methods and additional results may be found at:

References

- (1) Kojima, A.; Teshima, K.; Shirai, Y.; Miyasaka, T. Organometal Halide Perovskites as Visible-Light Sensitizers for Photovoltaic Cells. *J. Am. Chem. Soc.* **2009**, *131*, 6050–6051.
- (2) Kim, H.-S.; Lee, C.-R.; Im, J.-H.; Lee, K.-B.; Moehl, T.; Marchioro, A.; Moon, S.-J.; Humphry-Baker, R.; Yum, J.-H.; Moser, J. E.; *et al.*, Lead Iodide Perovskite Sensitized All-Solid-State Submicron Thin Film Mesoscopic Solar Cell with Efficiency Exceeding 9%. *Sci. Rep.* **2012**, *2*, 591.
- (3) Lee, M. M.; Teuscher, J.; Miyasaka, T.; Murakami, T. N.; Snaith, H. J. Efficient Hybrid Solar Cells Based on Meso-Superstructured Organometal Halide Perovskites. *Science* **2012**, *338*, 643–647.
- (4) Snaith, H. J. Perovskites: The Emergence of a New Era for Low-Cost, High-Efficiency Solar Cells. *J. Phys. Chem. Lett.* **2013**, *4*, 3623–3630.
- (5) Burschka, J.; Pellet, N.; Moon, S.-J.; Humphry-Baker, R.; Gao, P.; Nazeeruddin, M. K.; Grätzel, M. Sequential Deposition as a Route to High-Performance Perovskite-Sensitized Solar Cells. *Nature* **2013**, *499*, 316–319.
- (6) Xing, G.; Mathews, N.; Sun, S.; Lim, S. S.; Lam, Y. M.; Grätzel, M.; Mhaisalkar, S.; Sum, T. C. Long-Range Balanced Electron- and Hole-Transport Lengths in Organic-Inorganic $\text{CH}_3\text{NH}_3\text{PbI}_3$. *Science* **2013**, *342*, 344–347.
- (7) Milot, R. L.; Eperon, G. E.; Snaith, H. J.; Johnston, M. B.; Herz, L. M. Temperature-Dependent Charge-Carrier Dynamics in $\text{CH}_3\text{NH}_3\text{PbI}_3$ Perovskite Thin Films. *Adv. Funct. Mater.* **2015**, *25*, 6218–6227.
- (8) Chen, Z.; Turedi, B.; Alsalloum, A. Y.; Yang, C.; Zheng, X.; Gereige, I.; AlSaggaf, A.;

- Mohammed, O. F.; Bakr, O. M. Single-Crystal MAPbI₃ Perovskite Solar Cells Exceeding 21% Power Conversion Efficiency. *ACS Energy Lett.* **2019**, *4*, 1258–1259.
- (9) Green, M. A.; Dunlop, E. D.; Hohl-Ebinger, J.; Yoshita, M.; Kopidakis, N.; Ho-Baillie, A. W. Solar Cell Efficiency Tables (Version 55). *Prog Photovolt* **2020**, *28*, 3–15.
- (10) Min, H.; Kim, M.; Lee, S.-U.; Kim, H.; Kim, G.; Choi, K.; Lee, J. H.; Seok, S. I. Efficient, Stable Solar Cells by using Inherent Bandgap of α -Phase Formamidinium Lead Iodide. *Science* **2019**, *366*, 749–753.
- (11) Su, T.-S.; Eickemeyer, F. T.; Hope, M. A.; Jahanbakhshi, F.; Mladenović, M.; Li, J.; Zhou, Z.; Mishra, A.; Yum, J.-H.; Ren, D.; *et al.*, Crown Ether Modulation Enables over 23% Efficient Formamidinium-Based Perovskite Solar Cells. *J. Am. Chem. Soc.* **2020**, *142*, 19980–19991.
- (12) Jung, E. H.; Jeon, N. J.; Park, E. Y.; Moon, C. S.; Shin, T. J.; Yang, T.-Y.; Noh, J. H.; Seo, J. Efficient, Stable and Scalable Perovskite Solar Cells using poly(3-hexylthiophene). *Nature* **2019**, *567*, 511–515.
- (13) Giustino, F.; Snaith, H. J. Toward Lead-Free Perovskite Solar Cells. *ACS Energy Lett.* **2016**, *1*, 1233–1240.
- (14) Morss, L. R.; Siegal, M.; Stenger, L.; Edelstein, N. Preparation of Cubic Chloro Complex Compounds of Trivalent Metals: Cs₂NAMCl₆. *Inorg. Chem.* **1970**, *9*, 1771–1775.
- (15) Meyer, G.; Gaebell, H. Halo-Elpasolites. IV. On Bromo-Elpasolites Cs₂B^IM^{III}Br₆, B^I = Li, Na; M^{III} = Sc, Y, La–Lu, In, V, Cr). *Z. Naturforsch. B* **1978**, *33*, 1476–1478.
- (16) Meyer, G. Halo-Elpasolites. VI. The First-Iodo-Elpasolites, CsB^IM^{III}I₆ (B^I=Li, Na). *Z. Naturforsch. B* **1980**, *35*, 268–276.

- (17) Volonakis, G.; Filip, M. R.; Haghighirad, A. A.; Sakai, N.; Wenger, B.; Snaith, H. J.; Giustino, F. Lead-Free Halide Double Perovskites via Heterovalent Substitution of Noble Metals. *J. Phys. Chem. Lett.* **2016**, *7*, 1254–1259.
- (18) Volonakis, G.; Haghighirad, A. A.; Milot, R. L.; Sio, W. H.; Filip, M. R.; Wenger, B.; Johnston, M. B.; Herz, L. M.; Snaith, H. J.; Giustino, F. Cs₂InAgCl₆: A New Lead-Free Halide Double Perovskite with Direct Band Gap. *J. Phys. Chem. Lett.* **2017**, *8*, 772–778.
- (19) Volonakis, G.; Haghighirad, A. A.; Snaith, H. J.; Giustino, F. Route to Stable Lead-Free Double Perovskites with the Electronic Structure of CH₃NH₃PbI₃: A Case for Mixed-Cation [Cs/CH₃NH₃/CH(NH₂)₂]₂InBiBr₆. *J. Phys. Chem. Lett.* **2017**, *8*, 3917–3924.
- (20) Volonakis, G.; Sakai, N.; Snaith, H. J.; Giustino, F. Oxide Analogs of Halide Perovskites and the New Semiconductor Ba₂AgIO₆. *J. Phys. Chem. Lett.* **2019**, *10*, 1722–1728.
- (21) Slavney, A. H.; Hu, T.; Lindenberg, A. M.; Karunadasa, H. I. A Bismuth-Halide Double Perovskite with Long Carrier Recombination Lifetime for Photovoltaic Applications. *J. Am. Chem. Soc.* **2016**, *138*, 2138–2141.
- (22) McClure, E. T.; Ball, M. R.; Windl, W.; Woodward, P. M. Cs₂AgBiX₆ (X = Br, Cl): New Visible Light Absorbing, Lead-Free Halide Perovskite Semiconductors. *Chem. Mater.* **2016**, *28*, 1348–1354.
- (23) Deng, Z.; Wei, F.; Sun, S.; Kieslich, G.; Cheetham, A. K.; Bristowe, P. D. Exploring the Properties of Lead-Free Hybrid Double Perovskites using a Combined Computational-Experimental Approach. *J. Mater. Chem. A* **2016**, *4*, 12025–12029.
- (24) Slavney, A. H.; Leppert, L.; Saldivar Valdes, A.; Bartesaghi, D.; Savenije, T. J.; Neaton, J. B.; Karunadasa, H. I. Small-Band-Gap Halide Double Perovskites. *Angew.* **2018**, *57*, 12765–12770.

- (25) Wei, F.; Deng, Z.; Sun, S.; Hartono, N. T. P.; Seng, H. L.; Buonassisi, T.; Bristowe, P. D.; Cheetham, A. K. Enhanced Visible Light Absorption for Lead-Free Double Perovskite $\text{Cs}_2\text{AgSbBr}_6$. *Chem. Commun.* **2019**, *55*, 3721–3724.
- (26) Filip, M. R.; Hillman, S.; Haghighirad, A. A.; Snaith, H. J.; Giustino, F. Band Gaps of the Lead-Free Halide Double Perovskites $\text{Cs}_2\text{BiAgCl}_6$ and $\text{Cs}_2\text{BiAgBr}_6$ from Theory and Experiment. *J. Phys. Chem. Lett.* **2016**, *7*, 2579–2585.
- (27) Greul, E.; Petrus, M. L.; Binek, A.; Docampo, P.; Bein, T. Highly Stable, Phase Pure $\text{Cs}_2\text{AgBiBr}_6$ Double Perovskite Thin Films for Optoelectronic Applications. *J. Mat. Chem. A* **2017**, *5*, 19972–19981.
- (28) Wu, C.; Zhang, Q.; Liu, Y.; Luo, W.; Guo, X.; Huang, Z.; Ting, H.; Sun, W.; Zhong, X.; Wei, S.; *et al.*, The Dawn of Lead-Free Perovskite Solar Cell: Highly Stable Double Perovskite $\text{Cs}_2\text{AgBiBr}_6$ Film. *Adv. Sci.* **2018**, *5*, 1700759.
- (29) Gao, W.; Ran, C.; Xi, J.; Jiao, B.; Zhang, W.; Wu, M.; Hou, X.; Wu, Z. High-Quality $\text{Cs}_2\text{AgBiBr}_6$ Double Perovskite Film for Lead-Free Inverted Planar Heterojunction Solar Cells with 2.2% Efficiency. *Chem. Phys. Chem.* **2018**, *19*, 1696–1700.
- (30) Igbari, F.; Wang, R.; Wang, Z.-K.; Ma, X.-J.; Wang, Q.; Wang, K.-L.; Zhang, Y.; Liao, L.-S.; Yang, Y. Composition Stoichiometry of $\text{Cs}_2\text{AgBiBr}_6$ Films for Highly Efficient Lead-Free Perovskite Solar Cells. *Nano Lett.* **2019**, *19*, 2066–2073.
- (31) Longo, G.; Mahesh, S.; Buizza, L. R. V.; Wright, A. D.; Ramadan, A. J.; Abdi-Jalebi, M.; Nayak, P. K.; Herz, L. M.; Snaith, H. J. Understanding the Performance-Limiting Factors of $\text{Cs}_2\text{AgBiBr}_6$ Double-Perovskite Solar Cells. *ACS Energy Lett.* **2020**, *5*, 2200–2207.
- (32) Yang, X.; Wang, W.; Ran, R.; Zhou, W.; Shao, Z. Recent Advances in $\text{Cs}_2\text{AgBiBr}_6$ -Based Halide Double Perovskites as Lead-Free and Inorganic Light Absorbers for Perovskite Solar Cells. *Energy Fuels* **2020**, *34*, 10513–10528.

- (33) Kung, P.-K.; Li, M.-H.; Lin, P.-Y.; Jhang, J.-Y.; Pantaler, M.; Lupascu, D. C.; Grancini, G.; Chen, P. Lead-Free Double Perovskites for Perovskite Solar Cells. *Solar RRL* **2020**, *4*, 1900306.
- (34) Volonakis, G.; Giustino, F. Surface Properties of Lead-Free Halide Double Perovskites: Possible Visible-Light Photo-Catalysts for Water Splitting. *Appl. Phys. Lett.* **2018**, *112*, 243901.
- (35) Zhou, L.; Xu, Y.-F.; Chen, B.-X.; Kuang, D.-B.; Su, C.-Y. Synthesis and Photocatalytic Application of Stable Lead-Free $\text{Cs}_2\text{AgBiBr}_6$ Perovskite Nanocrystals. *Small* **2018**, *14*, 1703762.
- (36) Pan, W.; Wu, H.; Luo, J.; Deng, Z.; Ge, C.; Chen, C.; Jiang, X.; Yin, W.-J.; Niu, G.; Zhu, L.; *et al.*, $\text{Cs}_2\text{AgBiBr}_6$ Single-Crystal X-ray Detectors with a Low Detection Limit. *Nat. Photonics* **2017**, *11*, 726–732.
- (37) Yang, B.; Pan, W.; Wu, H.; Niu, G.; Yuan, J.-H.; Xue, K.-H.; Yin, L.; Du, X.; Miao, X.-S.; Yang, X.; *et al.*, Heteroepitaxial Passivation of $\text{Cs}_2\text{AgBiBr}_6$ Wafers with Suppressed Ionic Migration for X-ray Imaging. *Nat. Commun.* **2019**, *10*, 1989.
- (38) Keshavarz, M.; Debroye, E.; Ottesen, M.; Martin, C.; Zhang, H.; Fron, E.; K  chler, R.; Steele, J. A.; Bremholm, M.; Van de Vondel, J.; *et al.*, Tuning the Structural and Optoelectronic Properties of $\text{Cs}_2\text{AgBiBr}_6$ Double-Perovskite Single Crystals through Alkali-Metal Substitution. *Adv. Mater.* **2020**, *32*, 2001878.
- (39) Wu, C.; Du, B.; Luo, W.; Liu, Y.; Li, T.; Wang, D.; Guo, X.; Ting, H.; Fang, Z.; Wang, S.; *et al.*, Highly Efficient and Stable Self-Powered Ultraviolet and Deep-Blue Photodetector Based on $\text{Cs}_2\text{AgBiBr}_6/\text{SnO}_2$ Heterojunction. *Adv. Opt. Mater.* **2018**, *6*, 1800811.
- (40) Yang, J.; Bao, C.; Ning, W.; Wu, B.; Ji, F.; Yan, Z.; Tao, Y.; Liu, J.-M.; Sum, T. C.;

- Bai, S.; *et al.*, Stable, High-Sensitivity and Fast-Response Photodetectors Based on Lead-Free $\text{Cs}_2\text{AgBiBr}_6$ Double Perovskite Films. *Adv. Opt. Mater.* **2019**, *7*, 1801732.
- (41) Yuan, W.; Niu, G.; Xian, Y.; Wu, H.; Wang, H.; Yin, H.; Liu, P.; Li, W.; Fan, J. In Situ Regulating the Order–Disorder Phase Transition in $\text{Cs}_2\text{AgBiBr}_6$ Single Crystal toward the Application in an X-Ray Detector. *Adv. Funct. Mater.* **2019**, *29*, 1900234.
- (42) Zelewski, S. J.; Urban, J. M.; Surrente, A.; Maude, D. K.; Kuc, A.; Schade, L.; Johnson, R. D.; Dollmann, M.; Nayak, P. K.; Snaith, H. J.; *et al.*, Revealing the Nature of Photoluminescence Emission in the Metal-Halide Double Perovskite $\text{Cs}_2\text{AgBiBr}_6$. *J. Mater. Chem. C* **2019**, *7*, 8350–8356.
- (43) Li, Z.; Kavanagh, S. R.; Napari, M.; Palgrave, R. G.; Abdi-Jalebi, M.; Andaji-Garmaroudi, Z.; Davies, D. W.; Laitinen, M.; Julin, J.; Isaacs, M. A.; *et al.*, Bandgap Lowering in Mixed Alloys of $\text{Cs}_2\text{Ag}(\text{Sb}_x\text{Bi}_{1-x})\text{Br}_6$ Double Perovskite Thin Films. *J. Mater. Chem. A* **2020**, *8*, 21780–21788.
- (44) Kubicki, D. J.; Saski, M.; MacPherson, S.; Gałkowski, K.; Lewiński, J.; Prochowicz, D.; Titman, J. J.; Stranks, S. D. Halide Mixing and Phase Segregation in $\text{Cs}_2\text{AgBiX}_6$ ($X = \text{Cl}, \text{Br}, \text{and I}$) Double Perovskites from Cesium-133 Solid-State NMR and Optical Spectroscopy. *Chem. Mater.* **2020**, *32*, 8129–8138.
- (45) Zhang, L.; Fang, Y.; Sui, L.; Yan, J.; Wang, K.; Yuan, K.; Mao, W. L.; Zou, B. Tuning Emission and Electron–Phonon Coupling in Lead-Free Halide Double Perovskite $\text{Cs}_2\text{AgBiCl}_6$ under Pressure. *ACS Energy Lett.* **2019**, *4*, 2975–2982.
- (46) Hutter, E. M.; Gélvez-Rueda, M. C.; Bartesaghi, D.; Grozema, F. C.; Savenije, T. J. Band-Like Charge Transport in $\text{Cs}_2\text{AgBiBr}_6$ and Mixed Antimony–Bismuth $\text{Cs}_2\text{AgBi}_{1-x}\text{Sb}_x\text{Br}_6$ Halide Double Perovskites. *ACS Omega* **2018**, *3*, 11655–11662.
- (47) Bartesaghi, D.; Slavney, A. H.; Gélvez-Rueda, M. C.; Connor, B. A.; Grozema, F. C.;

- Karunadasa, H. I.; Savenije, T. J. Charge Carrier Dynamics in $\text{Cs}_2\text{AgBiBr}_6$ Double Perovskite. *J. Phys. Chem. C* **2018**, *122*, 4809–4816.
- (48) Karakus, M.; Jensen, S. A.; D’Angelo, F.; Turchinovich, D.; Bonn, M.; Cánovas, E. Phonon–Electron Scattering Limits Free Charge Mobility in Methylammonium Lead Iodide Perovskites. *J. Phys. Chem. Lett.* **2015**, *6*, 4991–4996, PMID: 26619006.
- (49) Shi, D.; Adinolfi, V.; Comin, R.; Yuan, M.; Alarousu, E.; Buin, A.; Chen, Y.; Hoogland, S.; Rothenberger, A.; Katsiev, K.; *et al.*, Low Trap-State Density and Long Carrier Diffusion in Organolead Trihalide Perovskite Single Crystals. *Science* **2015**, *347*, 519–522.
- (50) Dong, Q.; Fang, Y.; Shao, Y.; Mulligan, P.; Qiu, J.; Cao, L.; Huang, J. Electron-Hole Diffusion Lengths Greater than $175\ \mu\text{m}$ in Solution-Grown $\text{CH}_3\text{NH}_3\text{PbI}_3$ Single Crystals. *Science* **2015**, *347*, 967–970.
- (51) Saidaminov, M. I.; Abdelhady, A. L.; Murali, B.; Alarousu, E.; Burlakov, V. M.; Peng, W.; Dursun, I.; Wang, L.; He, Y.; Maculan, G.; *et al.*, High-Quality Bulk Hybrid Perovskite Single Crystals within Minutes by Inverse Temperature Crystallization. *Nat. Commun.* **2015**, *6*, 7586.
- (52) Shrestha, S.; Matt, G. J.; Osvet, A.; Niesner, D.; Hock, R.; Brabec, C. J. Assessing Temperature Dependence of Drift Mobility in Methylammonium Lead Iodide Perovskite Single Crystals. *J. Phys. Chem. C* **2018**, *122*, 5935–5939.
- (53) Ponce, S.; Schlipf, M.; Giustino, F. Origin of Low Carrier Mobilities in Halide Perovskites. *ACS Energy Lett.* **2019**, *4*, 456–463.
- (54) Steele, J. A.; Puech, P.; Keshavarz, M.; Yang, R.; Banerjee, S.; Debroye, E.; Kim, C. W.; Yuan, H.; Heo, N. H.; Vanackén, J.; *et al.*, Giant Electron–Phonon Coupling and Deep Conduction Band Resonance in Metal Halide Double Perovskite. *ACS Nano* **2018**, *12*, 8081–8090.

- (55) Yin, Y.; Tian, W.; Leng, J.; Bian, J.; Jin, S. Carrier Transport Limited by Trap State in $\text{Cs}_2\text{AgBiBr}_6$ Double Perovskites. *J. Phys. Chem. Lett.* **2020**, *11*, 6956–6963, PMID: 32787195.
- (56) Poncé, S.; Li, W.; Reichardt, S.; Giustino, F. First-Principles Calculations of Charge Carrier Mobility and Conductivity in Bulk Semiconductors and Two-Dimensional Materials. *Rep. Prog. Phys.* **2020**, *83*, 036501.
- (57) Giannozzi, P.; Baroni, S.; Bonini, N.; Calandra, M.; Car, R.; Cavazzoni, C.; Ceresoli, D.; Chiarotti, G. L.; Cococcioni, M.; Dabo, I.; *et al.*, QUANTUM ESPRESSO: a Modular and Open-Source Software Project for Quantum Simulations of Materials. *J. Phys. Condens. Matter* **2009**, *21*, 395502.
- (58) Poncé, S.; Margine, E.; Verdi, C.; Giustino, F. EPW: Electron–Phonon Coupling, Transport and Superconducting Properties using Maximally Localized Wannier Functions. *Comput. Phys. Commun* **2016**, *209*, 116–133.
- (59) Li, W. Electrical Transport Limited by Electron-Phonon Coupling from Boltzmann Transport Equation: An Ab Initio Study of Si, Al, and MoS_2 . *Phys. Rev. B* **2015**, *92*, 075405.
- (60) Poncé, S.; Margine, E. R.; Giustino, F. Towards Predictive Many-body Calculations of Phonon-Limited Carrier Mobilities in Semiconductors. *Phys. Rev. B* **2018**, *97*, 121201.
- (61) Schade, L.; Wright, A. D.; Johnson, R. D.; Dollmann, M.; Wenger, B.; Nayak, P. K.; Prabhakaran, D.; Herz, L. M.; Nicholas, R.; Snaith, H. J.; *et al.*, Structural and Optical Properties of $\text{Cs}_2\text{AgBiBr}_6$ Double Perovskite. *ACS Energy Lett.* **2019**, *4*, 299–305.
- (62) Klarbring, J.; Hellman, O.; Abrikosov, I. A.; Simak, S. I. Anharmonicity and Ultralow Thermal Conductivity in Lead-Free Halide Double Perovskites. *Phys. Rev. Lett.* **2020**, *125*, 045701.

- (63) Zelewski, S. J.; Urban, J. M.; Surrente, A.; Maude, D. K.; Kuc, A.; Schade, L.; Johnson, R. D.; Dollmann, M.; Nayak, P. K.; Snaith, H. J.; *et al.*, Revealing the Nature of Photoluminescence Emission in the Metal-Halide Double Perovskite $\text{Cs}_2\text{AgBiBr}_6$. *J. Mater. Chem. C* **2019**, *7*, 8350–8356.
- (64) Gray, M. B.; McClure, E. T.; Woodward, P. M. $\text{Cs}_2\text{AgBiBr}_{6-x}\text{Cl}_x$ Solid Solutions - Band Gap Engineering with Halide Double Perovskites. *J. Mater. Chem. C* **2019**, *7*, 9686–9689.
- (65) Lindquist, K. P.; Mack, S. A.; Slavney, A. H.; Leppert, L.; Gold-Parker, A.; Stebbins, J. F.; Salleo, A.; Toney, M. F.; Neaton, J. B.; Karunadasa, H. I. Tuning the Bandgap of $\text{Cs}_2\text{AgBiBr}_6$ through Dilute Tin Alloying. *Chem. Sci.* **2019**, *10*, 10620–10628.
- (66) Ji, F.; Klarbring, J.; Wang, F.; Ning, W.; Wang, L.; Yin, C.; Figueroa, J. S. M.; Christensen, C. K.; Etter, M.; Ederth, T.; *et al.*, Lead-Free Halide Double Perovskite $\text{Cs}_2\text{AgBiBr}_6$ with Decreased Band Gap. *Angew.* **2020**, *59*, 15191–15194.
- (67) Du, K.-z.; Meng, W.; Wang, X.; Yan, Y.; Mitzi, D. B. Bandgap Engineering of Lead-Free Double Perovskite $\text{Cs}_2\text{AgBiBr}_6$ through Trivalent Metal Alloying. *Angew.* **2017**, *56*, 8158–8162.
- (68) Savory, C. N.; Walsh, A.; Scanlon, D. O. Can Pb-Free Halide Double Perovskites Support High-Efficiency Solar Cells? *ACS Energy Lett.* **2016**, *1*, 949–955.
- (69) Yin, H.; Xian, Y.; Zhang, Y.; Li, W.; Fan, J. Structurally Stabilizing and Environment Friendly Triggers: Double-Metallic Lead-Free Perovskites. *Sol. RRL* **2019**, *3*, 1900148.
- (70) Feng, H.-J.; Deng, W.; Yang, K.; Huang, J.; Zeng, X. C. Double Perovskite Cs_2BBiX_6 (B = Ag, Cu; X = Br, Cl)/ TiO_2 Heterojunction: An Efficient Pb-Free Perovskite Interface for Charge Extraction. *J. Phys. Chem. C* **2017**, *121*, 4471–4480.

- (71) Filip, M. R.; Verdi, C.; Giustino, F. GW Band Structures and Carrier Effective Masses of $\text{CH}_3\text{NH}_3\text{PbI}_3$ and Hypothetical Perovskites of the Type APbI_3 : $\text{A} = \text{NH}_4$, PH_4 , AsH_4 , and SbH_4 . *J. Phys. Chem. C* **2015**, *119*, 25209–25219.
- (72) Kentsch, R.; Scholz, M.; Horn, J.; Schlettwein, D.; Oum, K.; Lenzer, T. Exciton Dynamics and Electron–Phonon Coupling Affect the Photovoltaic Performance of the $\text{Cs}_2\text{AgBiBr}_6$ Double Perovskite. *J. Phys. Chem. C* **2018**, *122*, 25940–25947.
- (73) Chapados, C.; Birnbaum, G. Infrared Absorption of SF_6 from 32 to 3000 cm^{-1} in the Gaseous and Liquid States. *J. Mol. Spectrosc.* **1988**, *132*, 323–351.
- (74) Verdi, C.; Giustino, F. Fröhlich Electron-Phonon Vertex from First Principles. *Phys. Rev. Lett.* **2015**, *115*, 176401.
- (75) Schade, L.; Mahesh, S.; Volonakis, G.; Zacharias, M.; Wenger, B.; Schmidt, F.; Kesava, S. V.; Prabhakaran, D.; Abdi-Jalebi, M.; Lenz, M.; *et al.*, Crystallographic, Optical, and Electronic Properties of the $\text{Cs}_2\text{AgBi}_{1-x}\text{In}_x\text{Br}_6$ Double Perovskite: Understanding the Fundamental Photovoltaic Efficiency Challenges. *ACS Energy Lett.* **2021**, *3*, 1073–1081.
- (76) Pistor, P.; Meyns, M.; Guc, M.; Wang, H.-C.; Marques, M. A.; Alcobé, X.; Cabot, A.; Izquierdo-Roca, V. Advanced Raman Spectroscopy of $\text{Cs}_2\text{AgBiBr}_6$ Double Perovskites and Identification of $\text{Cs}_3\text{Bi}_2\text{Br}_9$ Secondary Phases. *Scr. Mater.* **2020**, *184*, 24–29.
- (77) Poncé, S.; Jena, D.; Giustino, F. Hole Mobility of Strained GaN from First Principles. *Phys. Rev. B* **2019**, *100*, 085204.